AGU PUBLICATIONS

JGR

Journal of Geophysical Research: Solid Earth

RESEARCH ARTICLE

10.1002/2016JB013626

Key Points:
- Geodetic data show man-made subsidence in the geothermal fields in the Hengill area, Iceland, due to extraction of fluids
- Evidence that pressure drawdown is the driving mechanism behind the observed surface subsidence around the two Hengill power plants

Supporting Information:
- Table S1
- Table S2

Correspondence to:
D. Juncu,
daj22@hi.is

Citation:
Juncu, D., T. Árnadóttir, A. Hooper, and G. Gunnarsson (2017), Anthropogenic and natural ground deformation in the Hengill geothermal area, Iceland, *J. Geophys. Res. Solid Earth*, *122*, 692–709, doi:10.1002/2016JB013626.

Received 7 OCT 2016
Accepted 13 DEC 2016
Accepted article online 16 DEC 2016
Published online 28 JAN 2017

©2016. American Geophysical Union. All Rights Reserved.

Anthropogenic and natural ground deformation in the Hengill geothermal area, Iceland

D. Juncu[1], Th. Árnadóttir[1], A. Hooper[2], and G. Gunnarsson[3]

[1]Nordic Volcanological Center, Institute of Earth Sciences, University of Iceland, Reykjavík, Iceland, [2]COMET, School of Earth and Environment, University of Leeds, Leeds, UK, [3]OR—Reykjavík Energy, Reykjavík, Iceland

Abstract We investigate crustal deformation due to the extraction of water and steam from a high-enthalpy geothermal reservoir; a common occurrence, yet not well understood. The cause of this deformation can be a change in pressure or in temperature in the reservoir, both of which can be caused by extraction or injection of geothermal fluids. Our study area, the Hengill mountains in SW Iceland, is an active volcanic center and a plate triple junction that hosts two power plants producing geothermal energy. This combination of natural and anthropogenic processes causes a complex displacement field at the surface. We analyze geodetic data—Global Navigation Satellite System and Interferometric Synthetic Aperture Radar—to obtain the surface velocity field, which we then simulate using an inverse modeling approach. We focus on the deformation around the geothermal power plants but need to model the regional tectonic and volcanic deformation as well, because the signals are overlapping. We find that plate motion and a deep contracting body can explain the broad scale signal in the area. Local deformation near the two power plants, Hellisheidi and Nesjavellir, can be explained by extraction of geothermal fluids. We estimate reservoirs extending from 0.6 to 3.0 km depth at Hellisheidi, and 1.0 to 3.0 km depth at Nesjavellir for observed pressure decrease rates of 0.25 MPa/yr and 0.1 MPa/yr, respectively. We find that the main cause for the subsidence in the geothermal area is the observed pressure drawdown.

1. Introduction

Deformation of the Earth's crust caused by utilization of natural resources has been observed in many places. Examples include the following: exploitation of hydrocarbons [e.g., *Fielding et al.*, 1998], groundwater [e.g., *Chi and Reilinger*, 1984], and geothermal fluids [e.g., *Segall*, 1985; *Mossop and Segall*, 1997; *Allis and Zhan*, 2000; *Fialko and Simons*, 2000; *Keiding et al.*, 2010; *Vasco et al.*, 2013; *Jeanne et al.*, 2014; *Ali et al.*, 2016; *Drouin*, 2016; *Barbour et al.*, 2016]. Here we present a case study of crustal deformation driven by the use of a high-temperature geothermal field, a phenomenon that is not well understood. One challenge is to identify the cause of the deformation, as the volume change of a geothermal subsurface reservoir has been assumed to be caused mainly by (a) changes in pore/fracture pressure due to extraction or injection of fluids [e.g., *Allis and Zhan*, 2000; *Barbour et al.*, 2016] or (b) changes in temperature of the host rock due to production or injection [e.g., *Ali et al.*, 2016].

Mount Hengill is a volcanic system in SW Iceland, located on the plate boundary between the North American and Eurasian plates. More precisely, it marks the triple junction between the spreading-type Reykjanes Peninsula (RP), the Western Volcanic Zone (WVZ), and the transform-type South Iceland Seismic Zone (SISZ), see Figure 1. The volcanic basement hosts a high-temperature field harnessed by two power plants: Hellisheidi and Nesjavellir. The local geology is complex and composed of highly fractured interbedded hyaloclastite and lava formations [*Franzson et al.*, 2010; *Sæmundsson*, 1967]. There are many normal faults orientated along the SW-NE trending fissure swarm, as well as active N-S strike-slip faults [*Clifton et al.*, 2002].

Due to its vicinity to the SISZ, many earthquakes are recorded around Hengill. In May 2008 a seismic sequence with two M_W 6 earthquakes close to the Ölfus River (see Figure 2) occurred in the western end of the SISZ [*Hreinsdóttir et al.*, 2009]. Coseismic deformation from the two main events could be observed throughout the Hengill range [*Decriem et al.*, 2010] and postseismic deformation affected the surrounding areas during the years following the ruptures [*Geirsson et al.*, 2010]. The 2008 events are considered a continuation of a seismic sequence that started with two earthquakes in 2000 farther east in the SISZ, with moment magnitudes of 6.4–6.5 [e.g., *Árnadóttir et al.*, 2001; *Pedersen et al.*, 2003; *Decriem et al.*, 2010]. Earthquake sequences

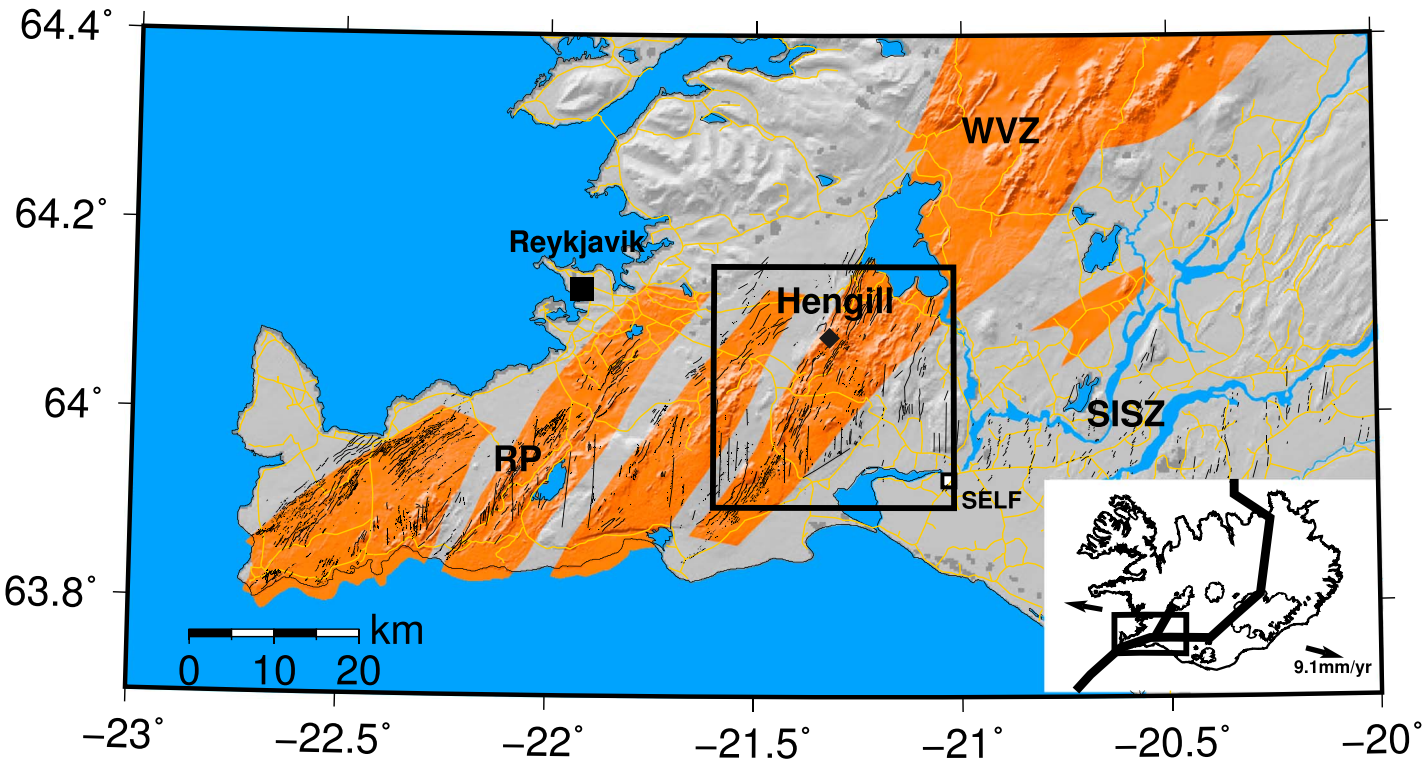

Figure 1. Southwest Iceland and the study area around Mount Hengill. Orange areas denote fissure swarms. Surface faults are shown as black lines and are taken from *Clifton et al.* [2002] and *Einarsson* [2008]. The small map of Iceland in the bottom right shows the location of plate boundaries taken from *Árnadóttir et al.* [2009] and plate velocities calculated using the MORVEL model [*DeMets et al.*, 2010].

in the SISZ recur at average intervals of 80–100 years, the last sequences in 1732–1734, 1784, and 1896 [*Einarsson*, 1991].

Hengill experienced volcanic unrest, with an increase in earthquake activity and uplift, between 1993 and 1998 [*Feigl et al.*, 2000; *Sigmundsson et al.*, 1997]. Seismic activity was strongly increased and climaxed in two earthquakes in June and November 1998 with magnitudes of M_W 5.4 and 5.1, respectively [*Vogfjörd and Slunga*, 2003; *Jakobsdóttir*, 2008]. *Feigl et al.* [2000] examined Interferometric Synthetic Aperture Radar (InSAR) data and found surface uplift rates of up to 19 mm/yr, which they interpreted to have been caused by pressure increase in a magma source at 7 km depth (shown with a yellow diamond in Figure 2).

Magmatic intrusions are the energy source for the geothermal fields in Hengill. Two power plants have been constructed to harness this resource. Nesjavellir has been operational since 1990 with an extraction rate of around 5 Mton/yr (water-steam mixture) in the first year and an average rate of around 16 Mton/yr in 2012–2015 [*Gunnlaugsson*, 2016a]. At Hellisheidi the production started in 2006 with a rate of 7 Mton/yr and was increased to an average rate of 38 Mton/yr in 2012–2015 [*Gunnlaugsson*, 2016b]. To maintain reservoir pressure, wastewater reinjection is being done at Hellisheidi, most of which around Húsmúli. The injection at this site received special attention for having triggered several earthquake swarms including two M_l 3.8 earthquakes in October 2011, a few weeks after it was initiated with a flow rate of around 550 l/s [*Halldorsson et al.*, 2012]. The total injection at Hellisheidi was on average 22 Mton in 2012–2015, of which 13 Mton were injected at Húsmúli [*Gunnlaugsson*, 2016b].

To gain a better understanding of the deformation in the Hengill area, we apply models that simulate the elastic response of the rock to pressure changes in the geothermal reservoir. We combine these models with a nonlinear inversion algorithm to find the best match of modeled and observed surface displacements. The problem in the Hengill area, however, is that there are several different processes that cause surface motion,

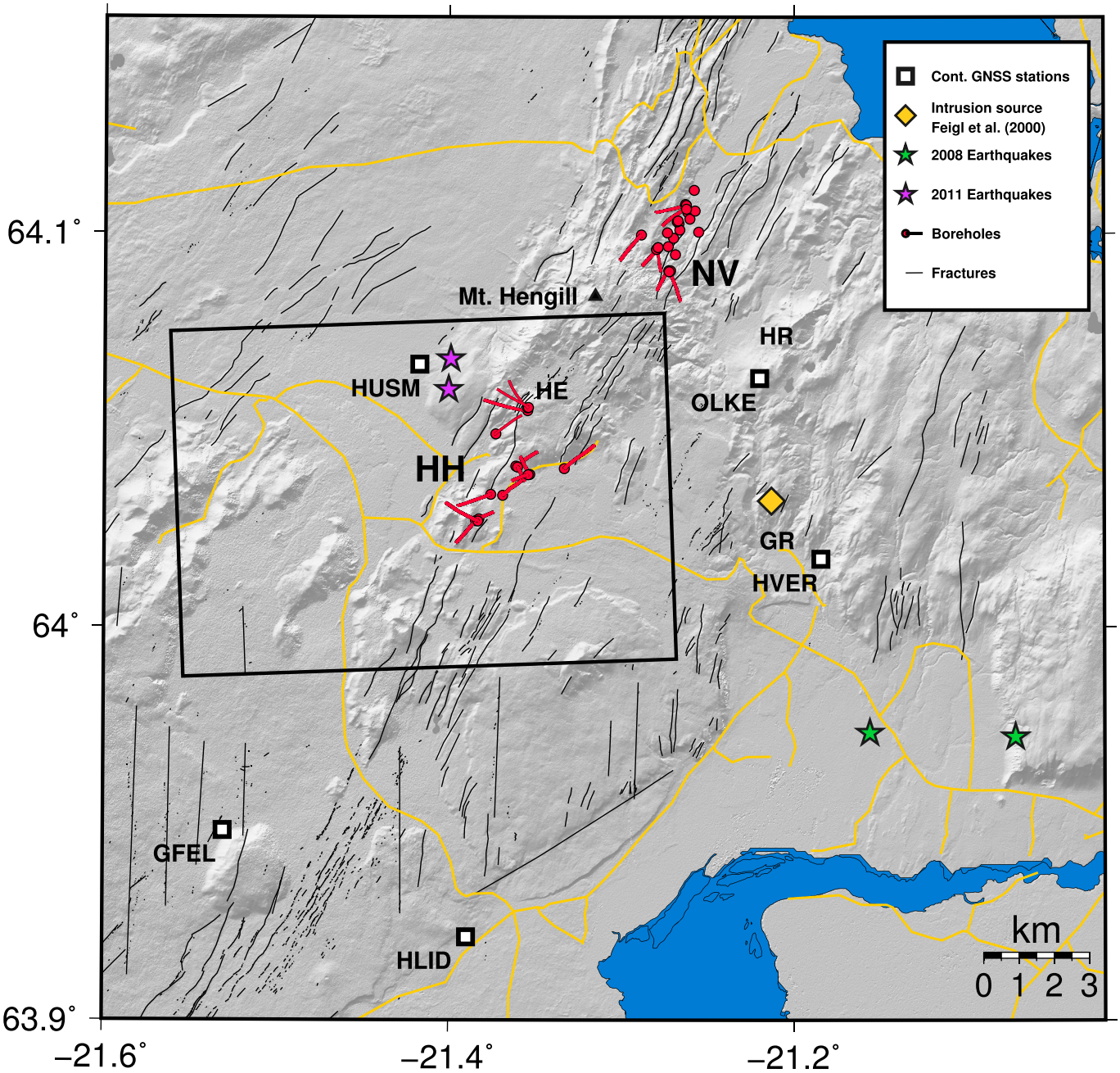

Figure 2. The Hengill area. HH denotes the Hellisheidi area, NV the Nesjavellir area. Continuous GNSS stations (white squares), mapped surface fractures (black lines) and the largest earthquakes in the area since 2008 (green and purple stars). The most productive boreholes at Hellisheidi and Nesjavellir are marked by red circles and lines. The black rectangle outlines the area of Figure 11. The three central volcanoes Hengill, Hrómundartindur, and Grensdalur are marked by HE, HR, and GR, respectively. The magmatic intrusion inferred by *Feigl et al.* [2000] is denoted with a yellow diamond.

in addition to the geothermal signal. In order to adequately study the local signals, we need a modeling approach that accounts for the regional deformation signal.

We concentrate our study on deformation during 2012–2015, as the production was fairly constant during this time. This also minimizes the influence of postseismic deformation from the two *M* 6 2008 earthquakes and excludes coseismic deformation from the two M_l 3.8 Húsmúli earthquakes in 2011. Also, we do not expect postseismic deformation from the small 2011 events after mid-2012, as confirmed by the continuous Global Navigation Satellite System (GNSS) station HUSM.

2. Observables

2.1. GNSS Data

We use two different modes of GNSS observations: continuous and campaign observations. With the former term we refer to GNSS stations that are installed in the field continuously and whose daily station positions we calculate from 24 h of measurements. Campaign stations were measured during annual campaigns (in 2012, 2013, 2014, and 2015) conducted by the Institute of Earth Sciences where stations are observed for at least 72 h. A dense GNSS network in Hengill was measured by Iceland Geosurvey (ÍSOR) in 2012, albeit with shorter observation sessions and less frequently. The station velocity estimates derived from data from the continuous stations are superior compared to those that are based on campaign data, because of the higher number of data points. Also, the accuracy of the positions derived from continuous measurements is higher, because position accuracy increases with deployment time, as error sources can be estimated more accurately [*Dzurisin*, 2007] and no changes in antenna height position are introduced. The campaign mode, however, is an important addition that helps increase the spatial density of the GNSS network.

In this study we use data from five continuous and 61 campaign stations (Figure 3). The data were analyzed with the GAMIT software, version 10.6 [*Herring et al.*, 2015]. We include data from continuous GNSS stations in Iceland and over 100 global reference stations to determine the daily solutions in the ITRF08 reference frame [*Altamimi et al.*, 2012]. We then used the GLOBK software, version 5.29 [*Herring et al.*, 2015], to estimate GNSS station positions and velocities in the study area, for the time interval 2012–2015 relative to stable North America (see Figure 3). We observe vertical and horizontal motion on the order of 10–25 mm/yr in the vicinity of the Hellisheidi power plant. The eastward oriented horizontal velocities in the south are mostly caused by spreading across the plate boundary between North America and Eurasia.

2.2. InSAR Data

In addition to the GNSS data set we use satellite-borne synthetic aperture radar (SAR) data, from the TerraSAR-X mission, track 41. We use the ascending (south-to-north orbit) data that the satellite acquires using a right looking configuration. Properties of satellite and orbit for track 41 can be found in Table 1. The SAR acquisitions are processed pairwise using interferometry—SAR interferometry is commonly denoted InSAR—essentially, measuring relative ground displacements (in the line of sight (LOS) of the satellite) through changes in phase between two images. In-depth theory on InSAR methodology can be found in, e.g., *Dzurisin* [2007].

We create interferograms with the DORIS software [*Kampes et al.*, 2003]. To account for topographic contributions we use the 25 m resolution intermediate TanDEM-X digital elevation model. Since we have access to multiple SAR acquisitions from a single track, we use a multitemporal InSAR approach [*Hooper*, 2008], in particular the small-baseline method which is implemented in the StaMPS software [*Hooper et al.*, 2012]. The algorithm uses a set of interferometric pairs (21 in our case) of a given track and identifies pixels that decorrelate little over short time intervals [*Hooper*, 2008]. Those pixels are then used to track the ground deformation over the time range of all acquisitions. StaMPS creates a time series of deformation (Figure 4) for these pixels and estimates an average velocity for the observation time. We use a subset of nine interferograms to estimate LOS velocities for the 2012–2015 time interval. The dates of the images that have been used for these interferograms are given in Table 2. In addition to being able to cover longer time spans, the multitemporal approach has the advantage of minimizing decorrelation noise. The average LOS unit vector for the imaged area is [−0.50 −0.12 0.86] (east, north, up) which implies that the measurements are mainly sensitive to vertical and E-W motion.

We remove the spatially correlated DEM (Digital Elevation Model) error from the interferograms and apply a linear correction to those interferograms we suspect are biased by variations in atmospheric delay [*Bekaert et al.*, 2015a]. The resulting time series plot is shown in Figure 4. Local deformation signals can be observed in the vicinity of both power plants and in the central east of the image. Regionally, we see a NW-SE gradient in deformation across the area, probably related to spreading across the plate boundary (see Figure 4).

Errors in the InSAR data are spatially correlated, which means that we need to find the full variance-covariance matrix to describe the error distribution of the InSAR velocity field v. To this end we follow the procedure of *Bekaert et al.* [2015b]. The method uses the variance of the difference in error between data points depending on their distance, i.e., a semivariogram, which can be extracted from the data set. Once the semivariogram is obtained, we calculate the data error covariance according to the analysis described in Appendix A.

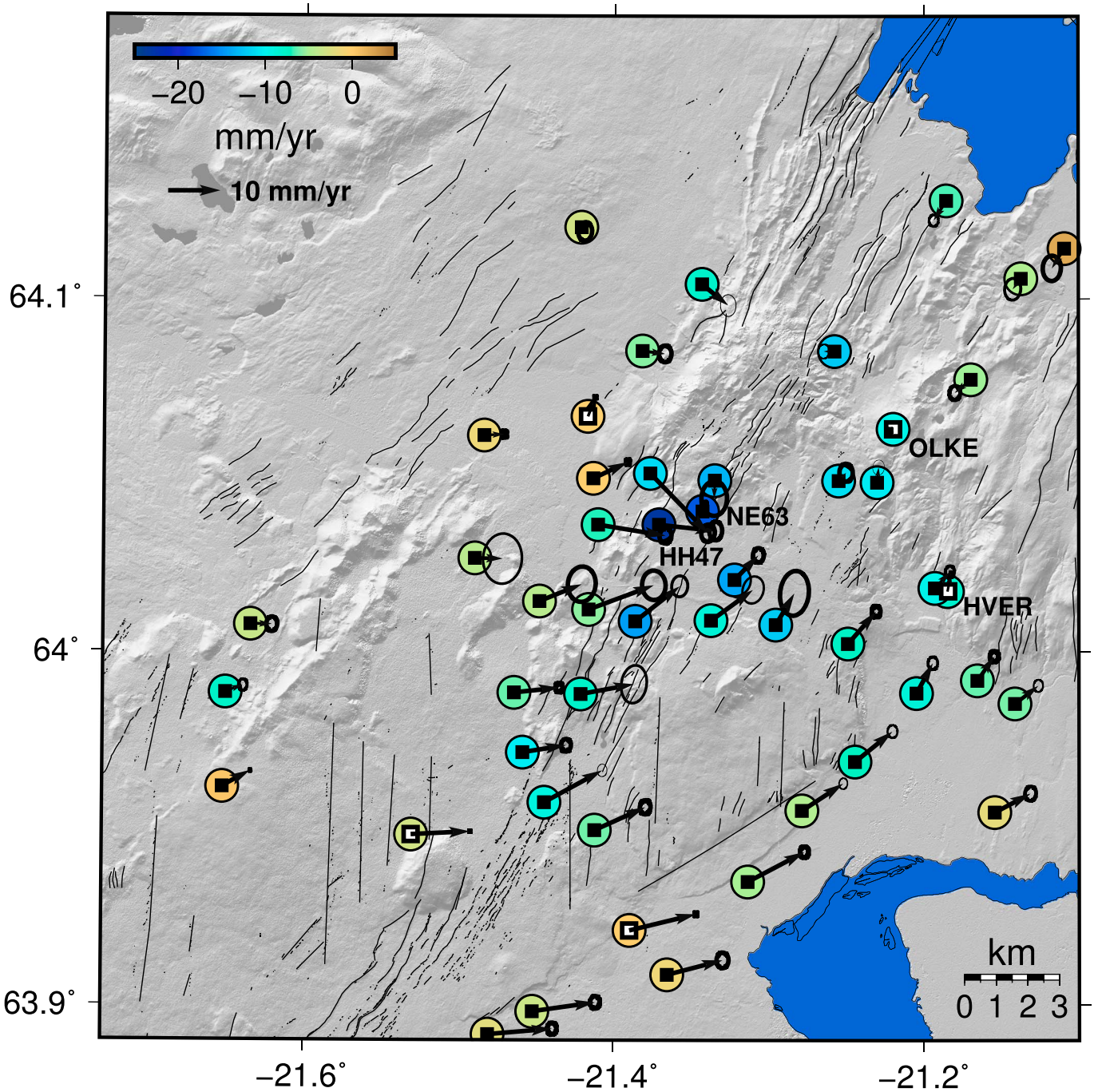

Figure 3. GNSS station velocities 2012–2015 relative to stable North America. Horizontal velocities are shown by arrows, with 95% confidence interval ellipses. Vertical velocities are shown by colored circles. Continuous GNSS stations are shown with white squares. The maximum vertical velocities are at campaign stations HH47 and NE63 with 23 and 18 mm/yr subsidence, respectively.

2.3. Production Data, Pressure, and Temperature Measurements

Reykjavík Energy and ÍSOR monitor pressure and temperature in several boreholes in the production area in Nesjavellir and Hellisheidi. Hellisheidi is the larger plant and had fairly constant production rates between 2012 and 2014 in the range of 40 Mton/yr. It was lower in the years before, however, and has also been reduced again to around 32 Mton/yr in 2015 [*Gunnlaugsson*, 2016b]. At Nesjavellir the production rate has been relatively constant between 2009 and 2015, in a range between 14 and 16 Mton/yr [*Gunnlaugsson*, 2016a].

Table 1. Configuration of Satellite and Orbit for TerraSAR-X Track 41

TerraSAR-X T41	Configuration
Heading	346°
Look direction	right
Look angle	27.2° – 29.5°
Altitude	515 km
Latitude	64.05°
Wavelength	31 mm (X band)
Resolution	3 m
Covered area	50 km × 30 km

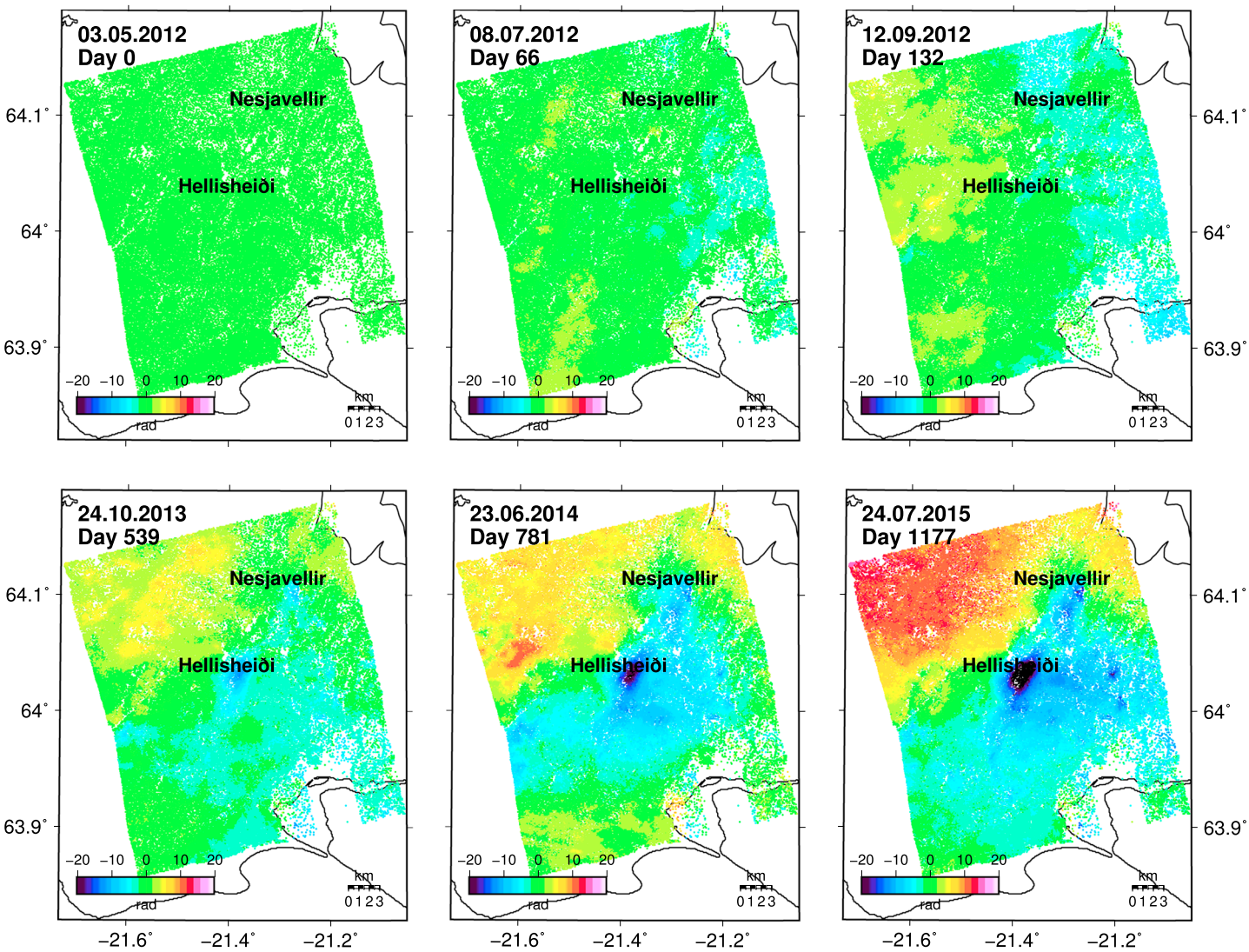

Figure 4. InSAR time series. Line of Sight (LOS) motion as change of phase observed from the satellite between 2012 and 2015. Negative phase values represent motion of the ground away from the satellite, positive values represent motion toward the satellite. Reference value is the mean value of the whole area.

Table 2. Interferometric Pairs of the SAR Acquisitions Used for Estimating the InSAR Velocity Field[a]

Interferogram	Δt (days)	b_p (m)
5/2012–7/2012	66	11.5
5/2012–9/2012	132	251.8
5/2012–10/2013	539	−82.5
7/2012–9/2012	66	240.3
7/2012–10/2013	473	−94.0
9/2012–10/2013	407	−334.3
10/2013–6/2014	242	176.4
10/2013–7/2015	638	110.0
6/2014–7/2015	396	−66.4

[a]The first column gives the month and year of the interferograms, second column the time interval, and the last column the perpendicular baseline.

Measurements of both pressure and temperature have been conducted in selected boreholes by ÍSOR [*Haraldsdóttir*, 2014; *Tryggvason*, 2014]. Rates of pressure drop seem to be consistently linear and range between 0.2 and 0.3 MPa/yr in the Hellisheidi region and 0.06 and 0.14 MPa/yr around Nesjavellir (Figure 5). The temperature measurements are less consistent. A linear rate of temperature decrease can be observed in, e.g., borehole HE-07 at 1100 m depth with around 3°C/yr. Temperature decrease is only observed in boreholes where the temperature is on the boiling point curve, the cooling being consistent with the pressure drop. This can be explained by absorption of latent heat due to pressure-induced boiling. The area most affected by this is the central part of the Hellisheidi field [*Gunnarsson et al.*, 2011].

3. Inverse Modeling

Our approach to modeling the observed deformation is using elastic half-space models relating subsurface processes to surface deformation. We embed these forward models in a nonlinear inversion framework to find a set of model parameters that can best reproduce the geodetic data. For the geothermal reservoirs we use the pressurized prolate spheroid model derived by *Yang et al.* [1988], which has been applied in comparable scenarios [*Fialko and Simons*, 2000; *Keiding et al.*, 2010]. This model consist of a pressurized body—representing a geothermal reservoir—emplaced in an elastic half-space (the Earth's crust). Pressure changes within the body cause stresses in the crust that result in deformation. For the broad scale deformation that occurs in eastern Hengill we assume a point source [*Mogi*, 1958]. We compare the calculated surface deformation with the observed deformation from our GNSS and InSAR data sets and adjust the source parameters to obtain the best agreement with the data. Following previous studies of deformation in geothermal areas we assume a shear modulus of $\mu = 10$ GPa and a Poisson's ratio of $\nu = 0.25$ [see *Fialko and Simons*, 2000; *Keiding et al.*, 2010].

The high number of InSAR data points ($\sim 10^4$) is impractical for the joint modeling of GNSS and InSAR data since it increases computation time and can create an imbalance in relative weights of the two data sets (the amount of GNSS measurements is on the order of 10^2). Therefore, we subsample the data set based on the variance of pixels with a quadtree algorithm [*Jónsson et al.*, 2002] to obtain a similar number of InSAR data as GNSS data. This method results in an InSAR data set that has a higher resolution in regions of larger displacement gradients and a lower resolution in regions with smaller gradients.

Since this is a nonlinear optimization problem with an infinite number of solutions, we apply a Bayesian optimization scheme. We use the cascading adaptive transitional metropolis in parallel (CATMIP) algorithm developed by *Minson et al.* [2013], a modified form of the Metropolis–Hastings algorithm [*Metropolis et al.*, 1953; *Hastings*, 1970], which is used to sample the posterior probability density function (PDF) of the model parameter space. It uses an annealing procedure similar to simulated annealing optimization [*Kirkpatrick et al.*, 1983]. During the annealing, the algorithm undergoes a succession of "cooling" steps, producing a new, intermediate PDF each time, until it reaches its final "temperature" which yields the optimal solution. At each step the samples from the previous stage are being resampled according to their relative likelihood, and each of

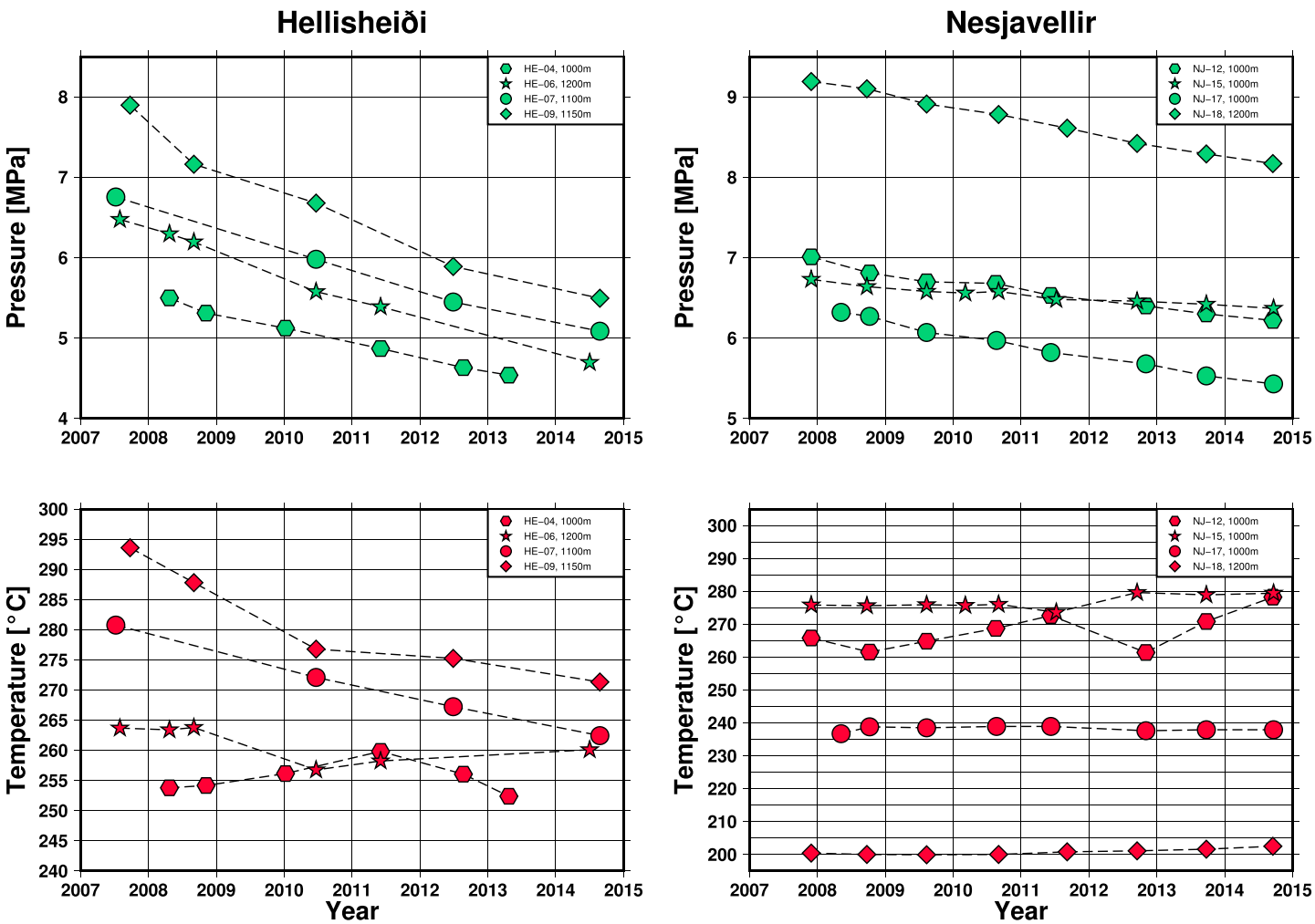

Figure 5. (top row) Pressure changes and (bottom row) temperature changes over time in different boreholes. (left column) Hellisheidi, (right column) Nesjavellir. Measurement depths are given in the legend. Data from Reykjavik Energy [*Gunnlaugsson*, 2016a, 2016b] and ÍSOR [*Haraldsdóttir*, 2014; *Tryggvason*, 2014].

those resamples serves as a seed for a separate Markov chain. This has the effect that more Markov chains are generated in regions of higher probability, which accelerates the algorithm toward the target posterior distribution.

The likelihood function $p(\mathbf{D}|\theta)$ lets us calculate the probability of the observed data $\mathbf{D}$ given a model θ,

$$p(\mathbf{D}|\theta) = \frac{1}{(2\pi)^{N_{\mathrm{dp}}/2}|\mathbf{C}|^{\frac{1}{2}}} e^{-\frac{1}{2}\mathbf{r}^{\mathrm{T}}\mathbf{C}^{-1}\mathbf{r}}, \tag{1}$$

where N_{dp} is the number of data points, $\mathbf{C}$ the covariance, and $\mathbf{r}$ the residual between observed and model data points. T is the matrix transpose.

The posterior PDF, $p(`|\mathbf{D})$, can be obtained following Bayes Theorem, which states that it is proportional to $p(\mathbf{D}|`)$:

$$p(\theta|\mathbf{D}) \propto p(\mathbf{D}|\theta)\, p(\theta), \tag{2}$$

where $p(`)$ is the prior PDF that describes the probability of each value of `. For a detailed description of the algorithm, see *Minson et al.* [2013].

4. Results

We model the observed geodetic data to learn more about the mechanisms that cause the deformation. In the Hengill area this a challenging problem because we observed signals from an interplay of tectonics,

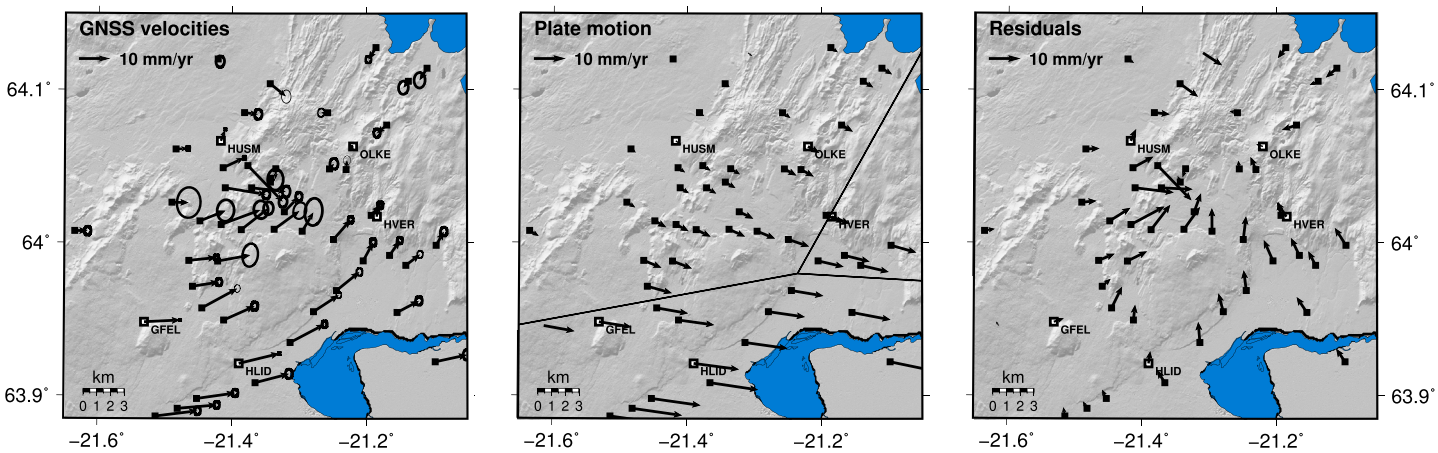

Figure 6. (left) GNSS horizontal velocities 2012–2015, (middle) predicted plate velocities using plate model from *Árnadóttir et al.* [2009] and (right) residual velocities. The velocities are shown relative to stable North America.

magmatism, and man-made deformation in two geothermal fields. The rate of plate spreading across Iceland is around 2 cm/yr and ~1 cm/yr in the study area. That is the same order of magnitude as the rate of subsidence in the vicinity of the power plants, which also causes horizontal motion toward the center of subsidence. The continuous GNSS stations OLKE and HVER as well as several campaign stations south of HVER are subsiding at a rate of up to 1 cm/yr (see Figure 3 and Table S1 in the supporting information), suggesting a wide area of subsidence probably indicating a deep source. Hence, we are aware of at least three different processes that cause deformation of similar magnitudes in the Hengill area. In order to estimate the deformation around the two power plants, we therefore also need to account for the plate spreading and broader scale deformation signal in the area. Our strategy is to first simplify the data set by correcting the horizontal velocities for the plate motion signal. Due to the limited aperture of the data in our study of Hengill and the number of local sources, we are not able to estimate the plate motion signal independently. We therefore choose to use a plate motion model from using the plate motion model from a study of country-wide GNSS motion by *Árnadóttir et al.* [2009]. In the Hengill area, the model consists of the obliquely spreading RP, the spreading WVZ, and the transform-type SISZ (see Figure 1). This allows us to better isolate the local geothermal signals as well as the broader signal in eastern Hengill, see Figures 6 and 7.

After substracting the plate motion from the InSAR data, the local deformation signals around the power plants become more distinct and the long wavelength NW–SE gradient is reduced (Figure 7). In the GNSS data,

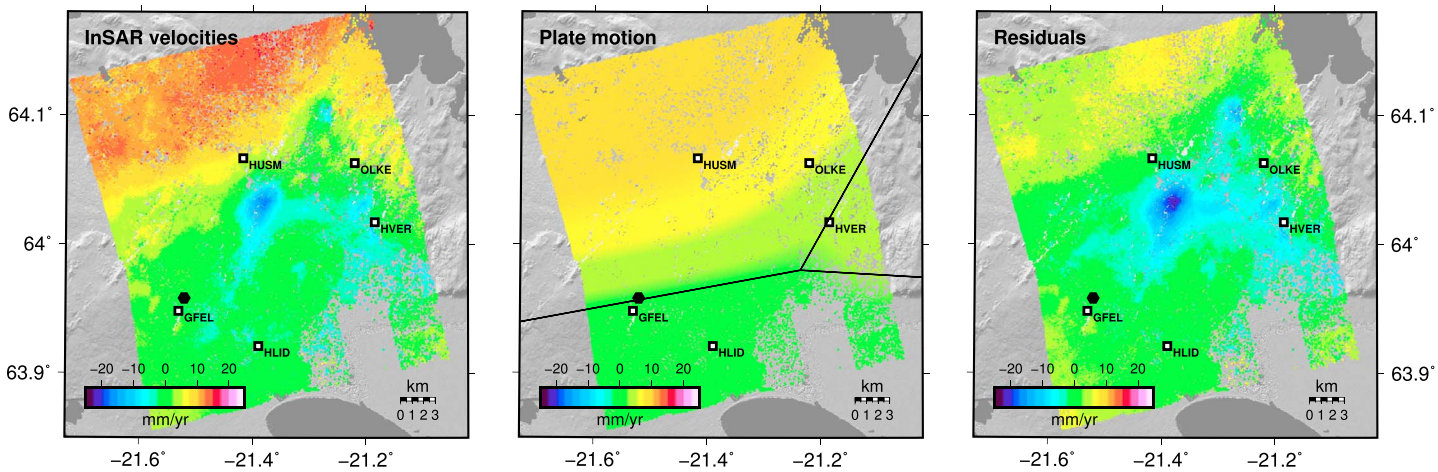

Figure 7. (left) InSAR mean velocity field for the 2012–2015 time interval derived from the time series shown in Figure 4, (middle) predicted plate velocity using plate model from *Árnadóttir et al.* [2009] and (right) residual velocities. The plate boundaries are plotted as black lines. All velocities are in LOS direction, positive toward the satellite, negative away from it. The black hexagon shows the location of the reference point of the velocities (v_{los} = 0).

Table 3. Estimated Parameters of the Deformation Sources and Their 90% Confidence Intervals (CI)[a]

Hellisheidi	Joint	90% CI	InSAR	90% CI	GNSS	90% CI
Hellisheidi						
Longitude (°W)	21.371	(21.365; 21.378)	21.376	(21.358; 21.389)	21.369	(21.358; 21.382)
Latitude (°N)	64.033	(64.030; 64.036)	64.032	(64.023; 64.038)	64.030	(64.020; 64.037)
Depth (km)	0.6	(0.3; 0.9)	0.7	(0.3; 2.5)	0.6	(0.2; 1.4)
Semimajor axis (km)	2.6	(1.9; 3.4)	2.5	(1.7; 5.4)	3.7	(2.3; 6.3)
Semiminor axis (km)	1.2	(1.0; 1.5)	1.1	(0.7; 1.5)	1.0	(0.7; 1.3)
Strike (deg)	46	(25; 68)	48	(16; 76)	31	(13; 60)
Nesjavellir						
Longitude (°W)	21.267	(21.254; 21.284)	21.274	(21.259; 21.288)	21.275	(21.255; 21.294)
Latitude (°N)	64.107	(64.092; 64.127)	64.097	(64.075; 64.122)	64.099	(64.077; 64.128)
Depth (km)	1.0	(0.1; 2.3)	0.8	(0.2; 1.9)	1.0	(0.1; 2.1)
Semimajor axis (km)	3.8	(1.9; 6.4)	3.7	(1.8; 6.3)	3.8	(1.9; 6.1)
Semiminor axis (km)	1.0	(0.4; 1.5)	0.8	(0.2; 1.3)	0.5	(0.1; 1.3)
Strike (deg)	22	(2; 66)	16	(2; 60)	33	(5; 80)
Eastern Hengill						
Longitude (°W)	21.247	(21.230; 21.267)	21.261	(21.129; 21.383)	21.251	(21.226; 21.274)
Latitude (°N)	64.057	(64.048; 64.066)	64.034	(64.004; 64.097)	64.060	(64.049; 64.070)
Depth (km)	6.9	(5.9; 8.1)	16.9	(11.9; 19.6)	7.2	(5.9; 8.5)
ΔV (10^6 m^3/yr)	−2.4	(-1.8; -3.1)	−16.1	(−1.8; −31.0)	−2.5	(−1.6; −3.4)

[a]The depths of the spheroidal sources at Hellisheidi and Nesjavellir are to the top of the body, the depth of the point source in eastern Hengill is to the center. The coordinates represent the center of the respective sources. The semimajor axis is half the long axis of the spheroid, orientated along its strike direction which is measured from the north. The semiminor axes are half the short axes of the spheroid, i.e., the vertical axis and the axis that is perpendicular to the strike. Pressure change is fixed at −0.25 MPa/yr (Hellisheidi) and −0.1 MPa/yr (Nesjavellir). We assume a shear modulus of $\mu = 10$ GPa and a Poisson's ratio of $\nu = 0.25$.

the horizontal velocities point toward Hengill (Figure 6), indicating a deep source in addition to the shallow geothermal sources.

Using only two geothermal sources, we obtain results that do not agree with the actual locations of the geothermal fields, because the nonlinear optimization tries to reduce residuals of the broad scale signal in eastern Hengill. By adding an unconstrained point source [*Mogi*, 1958] to the solution space, we obtain more

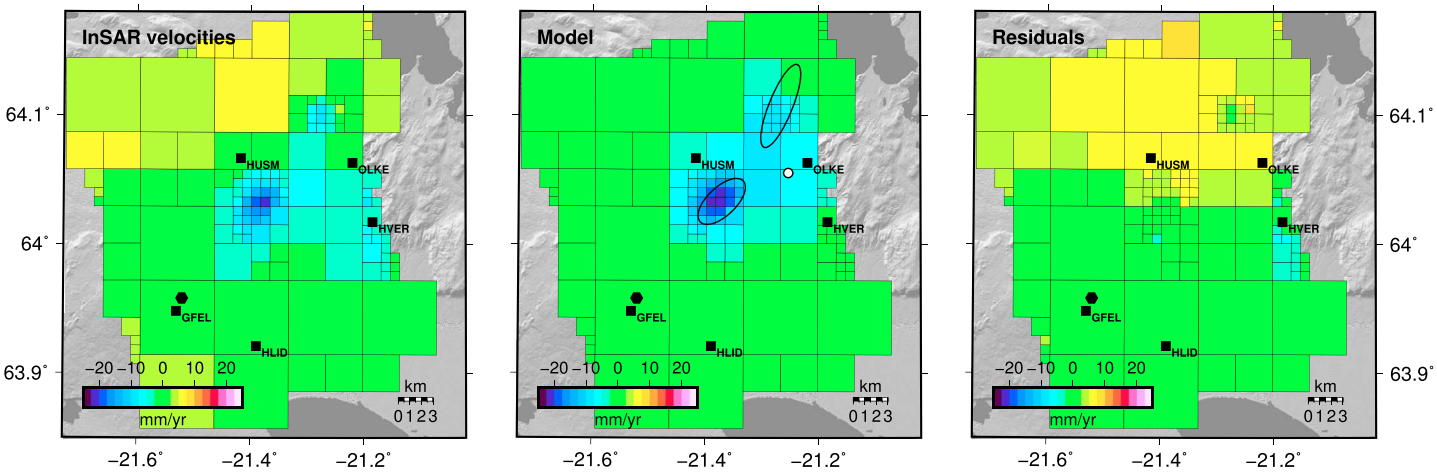

Figure 8. (left) Subsampled InSAR velocities 2012–2015 corrected for plate motion, (middle) estimated velocities, and (right) residuals. All in LOS of the satellite. The velocity reference point is denoted by a black hexagon. Black ellipses show surface projections of the spheroidal source locations, the white circle marks the point source.

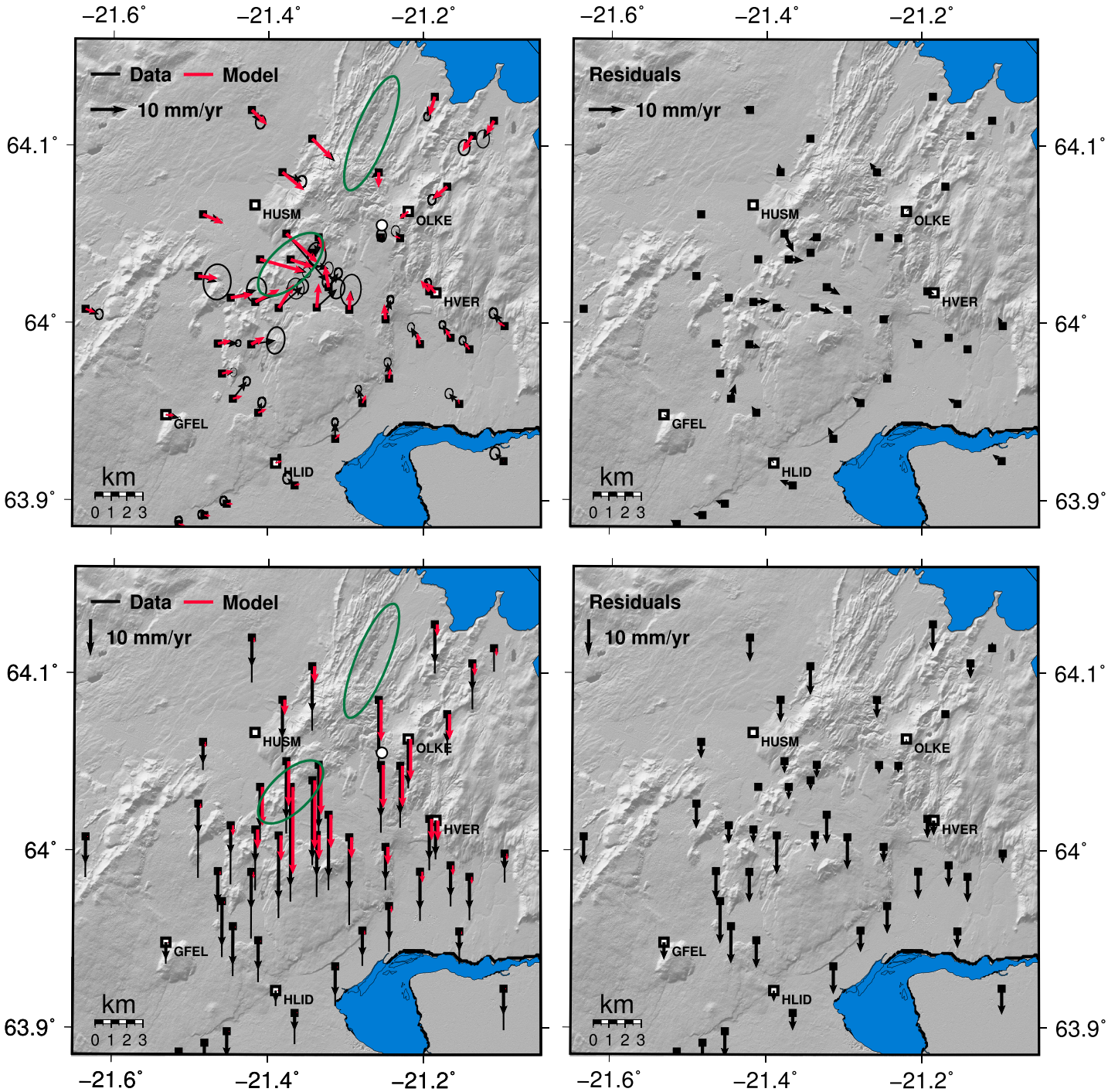

Figure 9. Observed GNSS station velocities after correcting for plate motion (black arrows) and estimated station velocities (red arrows) for the 2012–2015 time interval. (top row) Horizontal deformation corrected for plate motion using the ISNET model [*Árnadóttir et al.*, 2009]. (bottom row) Vertical deformation. Plots on the left-hand side show observed motion with black arrows and 95% confidence intervals and model predictions with red arrows. The plots on the right show residuals. All velocities are referenced to the continuous GNSS station SELF (see Figure 1). Dark green ellipsoids are geothermal source locations, the white circle depicts the deep point contraction source.

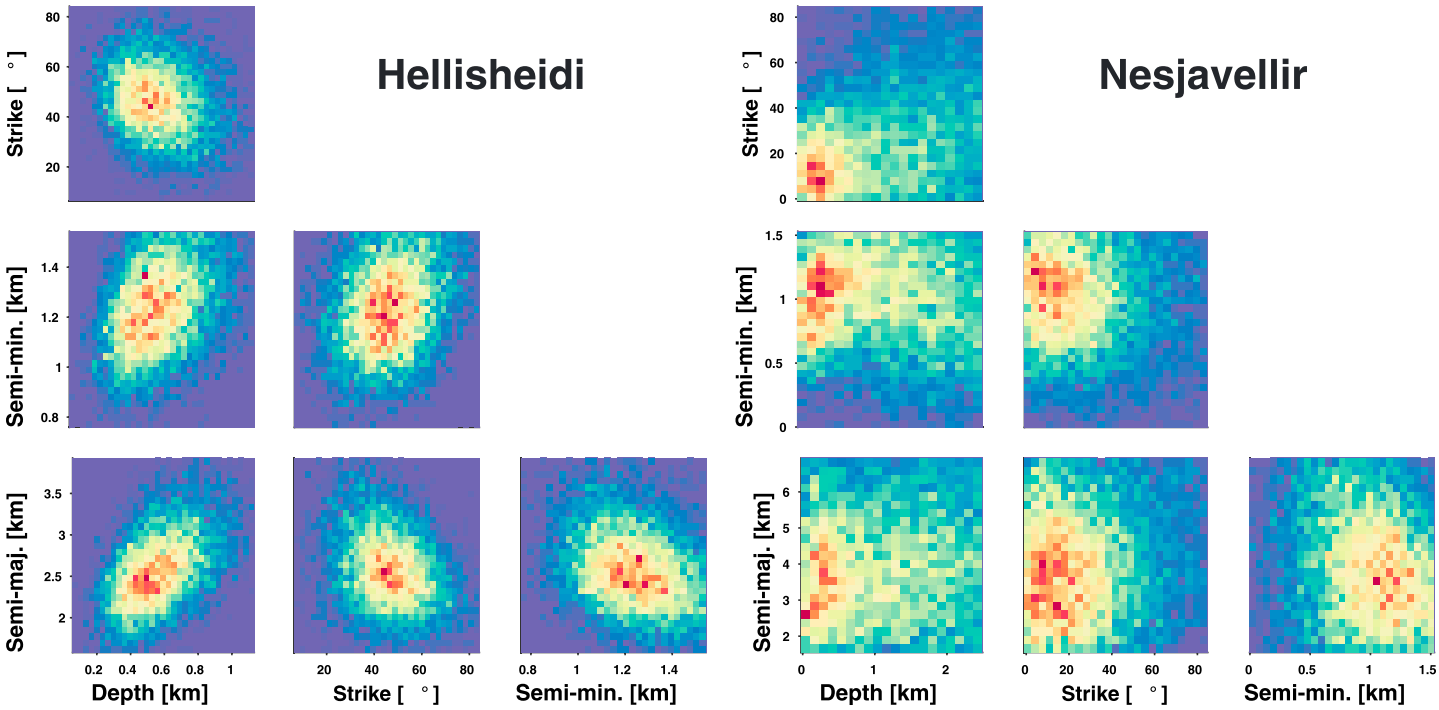

Figure 10. Posterior probability distribution for the model parameters of the spheroidal geothermal reservoirs. Depth is to the top of the reservoir. The coordinates represent the center of the respective sources. The semimajor axis is half the long axis of the spheroid, orientated along its strike direction which is measured from north. The semiminor axes are half the short axes of the spheroid, i.e., the vertical axis and the axis that is perpendicular to the strike. Pressure change is fixed at −0.25 MPa/yr (Hellisheidi) and −0.1 MPa/yr (Nesjavellir).

reasonable solutions for the geothermal sources and an additional deep source in eastern Hengill. For this source we obtain parameters (and 90% confidence intervals) of $6.9^{+1.2}_{-1.0}$ km depth and $2.4^{+0.7}_{-0.6}$ million m^3/yr volume decrease at the coordinates 64.057 ± 0.009°N and $21.253^{+0.020}_{-0.017}$°W (see Table 3). The location of this source falls into the area between the three central volcanoes of Hengill, Hrómundartindur, Hengill, and Grensdalur [*Feigl et al.*, 2000]. In this area both the InSAR data (see Figures 4 and 8) as well as the GNSS stations show significant displacement (subsidence rates of around 10 mm/yr at OLKE, HVER, and neighboring stations; see Figures 3 and 9). Our result is about ∼3 km NW of the magmatic intrusion suggested by *Feigl et al.* [2000] for the 1994–1998 uplift episode (which was 21.213°W/64.032°N/7.0 km depth). The proximity of the source locations suggests that the sources for the inflation and deflation are most likely related.

For the local signals around the geothermal power plants we use two spheroid-shaped pressure sources [*Yang et al.*, 1988]. We fix the pressure change at Hellisheidi to −0.25 MPa/yr which is the average rate of measured pressure decrease in the reservoir (see section 2.3). We find a shallow source of deformation (1.8 ± 0.4 km depth) below Hellisheidi with a volume of around 16 km^3 (Table 3). This translates to a decrease in reservoir volume ΔV of $4 \cdot 10^5$ m^3/yr using the relation given by *Eshelby* [1957]:

$$\Delta V = V \Delta P / \mu \,, \tag{3}$$

where V is the total reservoir volume, ΔP the change in pressure, and μ the shear modulus.

At Nesjavellir we fix the pressure change to −0.1 MPa/yr and find a reservoir with a depth of $2.0^{+1.4}_{-1.1}$ km and volume of around 17 km^3. The rate of volume decrease is approximately $2 \cdot 10^5$ m^3/yr. The source parameters are less well constrained than at Hellisheidi (Figure 10) due to fewer GNSS stations and low signal-to-noise ratio, compared to Hellisheidi.

It should be noted that the obtained volumes depend on the pressure change that is assumed for each reservoir. Considering the range of observed rates of pressure decay (see section 2.3), the reservoir volume at Hellisheidi may be as large as 17 km^3 (for a pressure change of −0.2 MPa/yr) or as low as 14 km^3 ($\Delta P = -0.3$ MPa/yr). At Nesjavellir the volume may range from 16 km^3 ($\Delta P = -0.14$ MPa/yr) to 18 km^3 ($\Delta P = -0.06$ MPa/yr). However, the uncertainties we obtain for the source dimensions (see Table 3) indicate even larger ranges for the total reservoir volumes.

The two spheroidal sources yield results that agree with the geodetic data within residuals of 5 mm/yr in the areas around the power plants. These models reproduce the regions of highest deformation in the InSAR data set (up to 26 mm/yr LOS velocity around the Hellisheidi power plant), as well as the largest GNSS velocities (Figure 3). At Hellisheidi, the model captures the maximum magnitude of the subsidence signal with residuals below 5 mm/yr and has a similarly SW-NE elongated shape. In the northeastern part of Hellisheidi field, however, the deformation is overestimated in the model when compared to the InSAR data (Figure 8). Around Nesjavellir the model has significant misfits, which can be seen in the InSAR data (Figure 8) and the vertical GNSS velocities of the stations further east of Nesjavellir (Figure 9). It may be that the Nesjavellir source is being overpredicted in order to accomodate the horizontal GNSS velocities.

The geothermal source models we obtain are shallow, which is consistent with the production depths in Hengill. Studies of other geothermal areas find similar source depths, e.g., depth ranges from 1 to 3 km for spheroidal sources in the Coso area in California [*Fialko and Simons*, 2000].

5. Discussion

Crustal deformation due to geothermal power production is mainly caused by contraction or expansion of the rock matrix in the reservoirs. It can be driven by changes in temperature as well as pressure, which may be in a feedback relation to each other. In order to keep the modeling simple, we first examine the effect of pressure change in our simulations and then use the results to evaluate whether this was a reasonable choice. We justify our choice with the fact that changes in pressure have been observed consistently throughout both reservoirs whereas temperature changes occur only in a few boreholes (see Figure 5). We use the measured reservoir pressure changes as a fixed parameter in our models and show that they can explain the deformation at Hellisheidi. This indicates that pressure changes are likely to be a key factor in the deformation.

5.1. Comparing Modeled Volume Changes to Extraction Rates

Pressure change can be translated into a change of reservoir volume, see equation (3). Other deformation studies have compared this model-estimated change of reservoir volume to volumetric fluid extraction rates, estimated from mass extraction rates given by the power plant operator [e.g., *Eysteinsson*, 2000; *Keiding et al.*, 2010; *Drouin*, 2016; *Barbour et al.*, 2016]. They often find discrepancy between estimated and observed volume change of more than 1 order of magnitude. This is not surprising since this approach is overly simplistic, mainly for two reasons: first, in a high-temperature geothermal field, the ratio of water to steam within the reservoir is not known. Thus, there is a large uncertainty when converting mass flow to volume flow. Second (and more importantly), the extracted fluid volume does not equal the total volume change of the reservoir. Instead, if we want to compare the change in rock volume to known production rates, we have to consider how they are related. For a reservoir with a volume V, the mass of produced fluid Δm can be related to the change in reservoir pressure ΔP through the *storativity* s of the rock, i.e., following *Axelsson* [2012]: $\Delta m = sV\Delta P$. Using equation (3) we can introduce the change in reservoir volume ΔV into this equation and find an expression that relates the mass extraction rate to the estimated ΔV (for spheroidal reservoirs)

$$\Delta m = s\mu\Delta V, \tag{4}$$

where μ is the shear modulus. Thus, in order to compare reservoir volume change to extraction rates, ideally, we should know the storativity. Since the storativity is not known in this case, we can only make a circular argument by solving for the value of s and then decide whether it is a reasonable value or not. To do this, we have to take into account that the mass extraction is balanced by natural recharge. According to reservoir models, we assume a total recharge rate for both Hellisheidi and Nesjavellir of 50% and then obtain a storativity of around $5 \cdot 10^{-6}$ kg m^{-3} Pa^{-1} for Hellisheidi (with $\Delta m = 18$ Mton/yr, $\Delta V = 4 \cdot 10^5$ m^3/yr and $\mu = 10$ GPa) and $4 \cdot 10^{-6}$ kg m^{-3} Pa^{-1} for Nesjavellir (with $\Delta m = 8$ Mton/yr, $\Delta V = 2 \cdot 10^5$ m^3/yr, and $\mu = 10$ GPa). These estimates of storativity are within the range of liquid-dominated reservoirs ($0.1-10 \cdot 10^{-6}$ kg m^{-3} Pa^{-1}, see Table 3 in *Axelsson* [2012]).

5.2. Impact of Thermal Contraction

Thermal contraction of the rock matrix might be another important contribution to the total deformation. We can use the observed rates of temperature drop to approximate the magnitude of deformation that we could expect from thermal contraction of the rock matrix. Observed temperature changes at the Hellisheidi power plant indicate a decrease of up to 3°C/yr in several boreholes, while others show no change (see Figure 5).

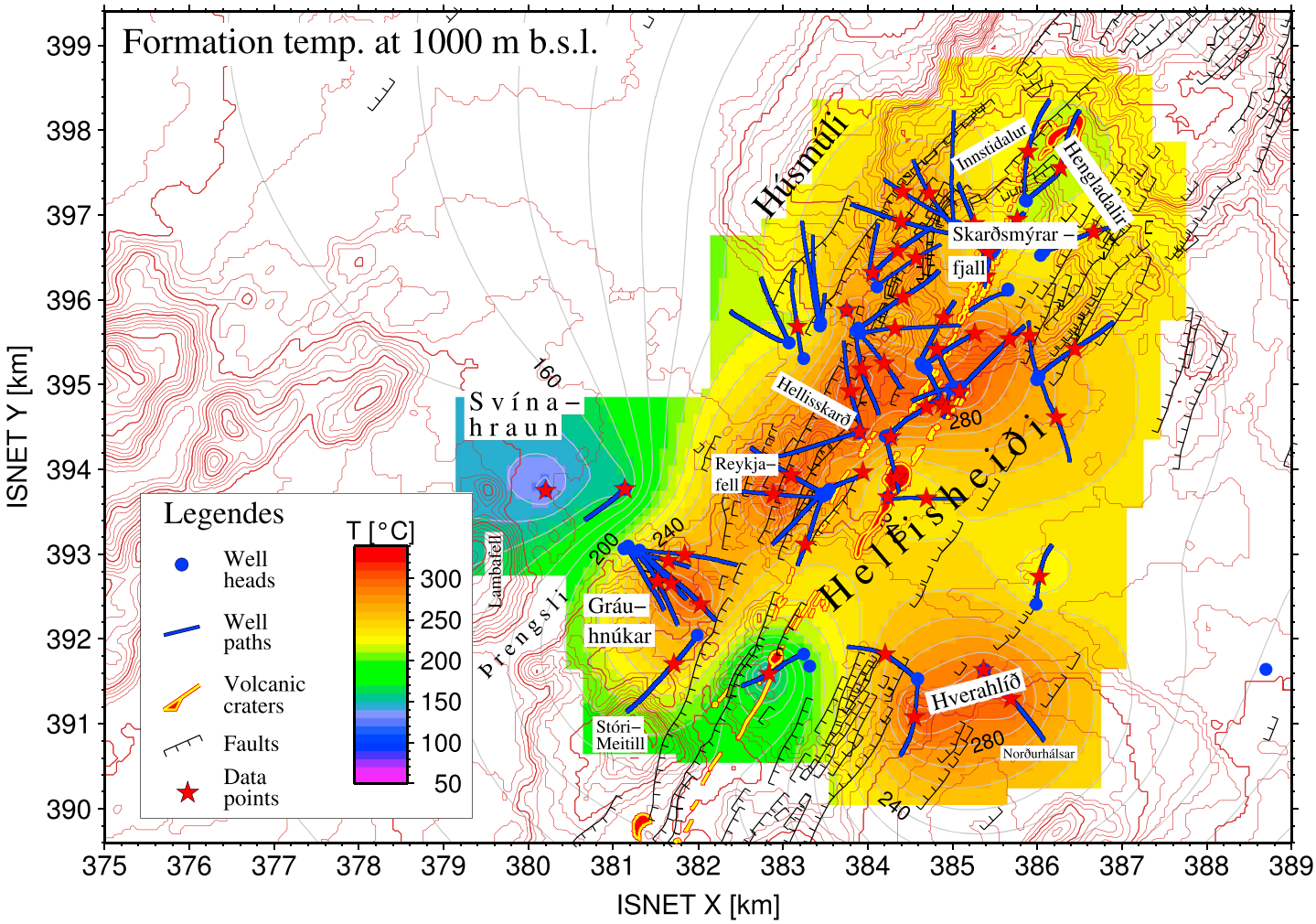

Figure 11. Temperature distribution, boreholes (blue dots and lines), and data points (red stars) in the Hellisheidi reservoir at 1000 m depth.

We assume that temperature is reduced mainly due to latent heat effects of boiling caused by dropping pressure, and this appears only in the part of the reservoir that has a combination of high temperatures and low pressures. These conditions can be found in the uppermost part of the central region of the reservoir (see Figure 11). We approximate the size of the area to 1.5 km^2 with a thickness of around 300 m. We use the thermal expansion relation $\Delta V_{\text{th}} = \alpha V \Delta T$ [*Turcotte and Schubert*, 2002]—where ΔT, V, and α are the temperature change, volume, and thermal expansion coefficient of the rock, respectively—to estimate the volume change due to thermal contraction, ΔV_{th}. Assuming a coefficient of thermal expansion (for a rock with basalt-like composition) of $\alpha = 2 \cdot 10^{-5}$°/C [*Robertson*, 1988] and a rock volume of 0.5 m^3 (see above), we obtain a contraction of about $3 \cdot 10^4$ m^3/yr. That is less than 10% of the volume change that we estimate for the spheroidal source at Hellisheidi (see section 4). This indicates that for this area, the deformation caused by temperature changes is probably minor when compared to deformation caused by changes in pressure.

5.3. Nature of the Deep Source in Eastern Hengill

We want to test if the subsidence observed in the eastern part of Hengill may be related to the intrusion that *Feigl et al.* [2000] inferred for the time interval 1994–1998. The total volume of injected magma inferred by *Feigl et al.* [2000] amounts to ~40 million m^3. If the whole volume would solidify after the intrusion, it would cause a subsequent volume decrease of 4 million m^3, assuming a density ratio between liquid and solid magma of 0.9 [*Caricchi et al.*, 2014]. Our modeling results (Table 3) imply a volume loss of 7 million m^3 over the time interval 2012–2015, which is larger than the estimate of the contraction of the intrusion due to solidification by a factor of around 2. The difference is likely to be even larger since there is probably contraction before and after the 2012–2015 time interval. The mismatch both in volumes and in source locations

(see section 4) could suggest that interpreting the inflation and deflation as solely caused by a magmatic intrusion and the cooling thereof might be—at least partly—incorrect. Other studies have shown that inflation in volcanic areas can be explained by natural hydrothermal fluid injection and gas formation [*Hurwitz et al.*, 2007; *Hutnak et al.*, 2009]. These processes yield a volume increase that is more reversible than one caused by magma injection alone, and thus may better explain the magnitude of deflation that we estimate. A distinct location for pore pressure-driven deformation would also be harder to constrain because of the mobility of the fluids, which might further explain the difference in modeled locations between inflation and deflation episodes. Furthermore, *Tryggvason et al.* [2002] conducted a seismic tomography study (using seismic data from 1973 to 1999) and found a low-velocity anomaly below Hengill, which they intepreted as evidence for the presence of supercritical fluids at depth. If close to the critical point, these fluids could have been the explanation for the inflation.

6. Conclusion

We obtain the surface deformation field in the Hengill region from 2012 to 2015 from both GNSS and SAR observations and correct the data for plate motion using the results from *Árnadóttir et al.* [2009]. We perform a joint inversion on the residual velocities using models of pressurized spheroids and spheres in an elastic half-space. The inversion shows that the remaining data can be reproduced by three deformation sources. We find two shallow spheroidal sources representing contracting geothermal reservoirs in the Hellisheidi and Nesjavellir production fields. We also estimate a deep contracting source below eastern Hengill in the vicinity of the 1994–1998 inflation source [*Feigl et al.*, 2000]. The results show how complex deformation signals can be in Iceland, where tectonic, magmatic, and anthropogenic deformation can overlap, and how important it is to take all these processes into account.

The eastern Hengill deformation source has a depth of $6.9^{+1.2}_{-1.0}$ km and a volume loss of around 2 million m^3/yr. We can not conclusively link it to the intrusion suggested by *Feigl et al.* [2000]. To better understand this signal, the whole deformation history since the end of the uplift episode should be considered. It may also be worthwhile to revisit the deformation data for the intrusive episode and investigate if it may be explained by processes other than magma intrusion, e.g., natural hydrothermal fluid injection, gas formation, or thermal expansion.

The Hellisheidi geothermal source model we estimate extends from about 0.6 to 3.0 km depth and is orientated roughly along the regional fissure swarm. The Nesjavellir source extends from about 1.0 to 3.0 km depth. This source is less well constrained than the Hellisheidi source, due to a lower GNSS station density and a weaker deformation signal.

Using the observed pressure change in the geothermal fields, we are able to reproduce the subsidence signal at the surface. Therefore, we argue that it is likely that the pressure decrease is responsible for most of the deformation observed in the geothermal areas.

Appendix A: The Variance-Covariance Matrix of the InSAR Data Set

For obtaining the variance-covariance matrix of the InSAR data we follow the procedure by *Bekaert et al.* [2015b]. We start with the variance of the difference of two correlated variables, which is given by

$$\sigma^2_{\mathrm{pq}} = \sigma^2_p + \sigma^2_q - 2\,C_{\mathrm{pq}}\,, \tag{A1}$$

where σ^2_{pq} is the difference in variances between any random pair of points, p and q, in the InSAR image, σ^2_{p} is the variance of point p, and C_{pq} is the covariance of points p and q, which is what we are interested in.

Now, if we assume all points by themselves have the same variance ($\sigma^2_p = \sigma^2_q$), equation (A1) reduces to that of a semivariogram,

$$\gamma_{\mathrm{pq}}(x) = \sigma^2_0 - C_{\mathrm{pq}}(x)\,, \tag{A2}$$

where x is the distance between points p and q, σ^2_0 is the variance at each point, and

$$\gamma_{\mathrm{pq}} = \frac{1}{2}\sigma^2_{\mathrm{pq}}\,. \tag{A3}$$

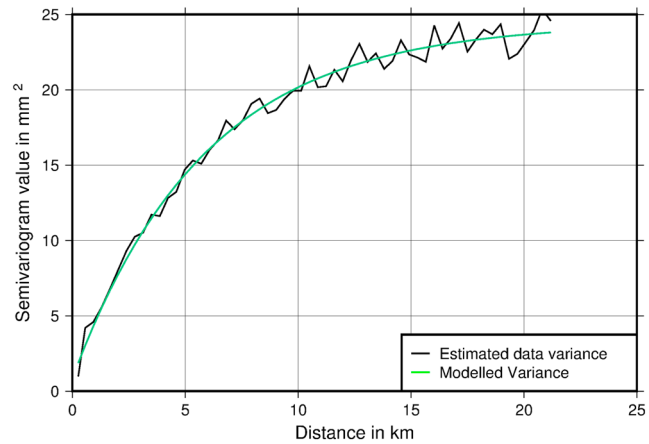

Figure A1. Semivariogram value over the distance between points. The model (green line) is calculated from equation (A6). $\sigma^2_{\text{bin}} = 23.6\ \text{mm}^2$, $N = 0.8\ \text{mm}^2$, $R = 17.5$ km.

We use a bootstrapping approach [see, e.g., *Efron and Tibshirani*, 1986] to calculate the right-hand side of equation (A3). To this end, we first compute the best estimate of the velocity field, $\hat{v}$, from the interferograms using weighted least squares based on the covariance between each of them. Then, we calculate n realizations of the velocity field v_{boot} by resampling from the set of interferograms. We can calculate the residuals between v_{boot} and $\hat{v}$ as,

$$r^k = v^k_{\text{boot}} - \hat{v}\,, \tag{A4}$$

where k represents one of the n bootstrap realizations.

Now, we can use the residuals to estimate the variance, σ^2_{pq}, between pairs of points,

$$\sigma^2_{\text{pq}} = \sum_k^n \frac{\left(r^k_{\text{pq}}\right)^2}{n-1}\,, \tag{A5}$$

where r^k_{pq} is the difference in r^k between a random pair of points p and q ($r^k_{\text{p}} - r^k_{\text{q}}$).

Binning σ^2_{pq} depending on distance between points yields the semivariogram which we can describe with a Gaussian semivariogram model,

$$\gamma_m(x) = N + \sigma^2_0\,(1 - \text{e}^{-3\frac{x}{R}})\,, \tag{A6}$$

where N is often called nugget term, representing variations on small spatial scale, R is the range, i.e., the distance limit after which data is no longer correlated and the variance σ^2_0 is also known as the sill. Using the binned variances, we can estimate N, σ^2_0 and R, plug σ^2_0 and γ into equation (A2) and solve it for C_{pq}. Then we can calculate the variance-covariance matrix of our data as follows:

$$C_{\text{pq}}(x) = \sigma^2_{\text{bin}} \cdot e^{-3\frac{x}{R}} - N\,, \tag{A7}$$

Using the estimated semivariogram of our data (see Figure A1), we use the model of equation (A2) and invert for the values of N, σ^2_0, and R: $\sigma^2_{\text{bin}} = 23.6\ \text{mm}^2$, $N = 0.8\ \text{mm}^2$, $R = 17.5$ km. From here we calculate the variance-covariance matrix of our data using equation (A7). These estimates give a standard deviation of the InSAR data of 4.9 mm/yr.

Acknowledgments
The authors would like to thank Einar Gunnlaugsson from Reykjavik Energy (RE) for providing production data from Hellisheidi and Nesjavellir; Bjarni Reyr Kristjánsson (RE) for discussions and advice regarding the geothermal power plant operations; RE and ÍSOR for GNSS data from the dense Hengill network; the Icelandic Meteorological Office (IMO) for operating the cGPS network in Iceland; Sigrún Hreinsdóttir (GNS, New Zealand) for global GNSS solutions; Tabrez Ali (University of Wisconsin, Madison, USA) for help and ideas regarding deformation in geothermal areas; Halldór Geirsson (IES) for helpful comments on the work in progress; Sarah Minson (U.S. Geological Survey) for help with CATMIP and letting us use her code; David Bekaert (University of Leeds, UK) for helpful advice on the InSAR processing; Sigurjón Jónsson (King Abdullah University of Science and Technology, KSA) for providing his Quadtree code; Guðni Axelsson (ÍSOR) for helpful discussions concerning geothermal reservoirs; the crustal deformation group at IES for help with the GNSS measurements in SW Iceland and discussions on the work in progress. For computing the elastic half-space models we use *DMODELS* [*Battaglia et al.*, 2013]. Many of the figures were prepared using the GMT software [*Wessel and Smith*, 1991; *Wessel et al.*, 2013]. The earthquake locations in Figure 2 were provided by IMO. The intermediate TanDEM-X digital elevation model used in the InSAR processing was provided by DLR under project IDEM_GEOL0123. COMET is the NERC Centre for the Observation and Modelling of Earthquakes, Volcanoes and Tectonics. This work was supported in part by grants from the Iceland Research Fund and the University of Iceland Research Fund. The data for this paper are available by contacting the corresponding author at daj22@hi.is.

References

Ali, S., et al. (2016), Time-series analysis of surface deformation at Brady Hot Springs geothermal field (Nevada) using interferometric synthetic aperture radar, *Geothermics*, *61*, 114–120.
Allis, R., and X. Zhan (2000), Predicting subsidence at Wairakei and Ohaaki geothermal fields, New Zealand, *Geothermics*, *29*, 479–497.
Altamimi, Z., I. Metivier, and X. Collileux (2012), ITRF2008 plate motion model, *J. Geophys. Res.*, *117*, B07402, doi:10.1029/2011JB008930.
Árnadóttir, T., S. Hreinsdóttir, G. Gudmundsson, P. Einarsson, M. Heinert, and C. Völksen (2001), Crustal deformation measured by GPS in the South Iceland Seismic Zone due to two large earthquakes in June 2000, *Geophys. Res. Lett.*, *28*(21), 4031–4033.
Árnadóttir, T., B. Lund, W. Jiang, H. Geirsson, H. Björnsson, P. Einarsson, and T. Sigurdsson (2009), Glacial rebound and plate spreading: Results from the first countrywide GPS observations in Iceland, *Geophys. J. Int.*, *177*, 691–716.

Axelsson, G. (2012), The physics of geothermal energy, in *Comprehensive Renewable Energy*, edited by A. Sayigh, pp. 3–50, Elsevier, Oxford, U. K.

Barbour, A. J., E. L. Evans, S. H. Hickman, and M. Eneva (2016), Subsidence rates at the southern Salton Sea consistent with reservoir depletion, *J. Geophys. Res. Solid Earth*, *121*, 5308–5327, doi:10.1002/2016JB012903.

Battaglia, M., P. Cervelli, and J. Murray (2013), Modeling crustal deformation near active faults and volcanic centers—A catalog of deformation models, U.S. Geol. Surv. Tech. and Meth. 13-B1, 96 p., USGS, Reston, Va.

Bekaert, D., R. Walters, T. Wright, A. Hooper, and D. Parker (2015a), Statistical comparison of InSAR tropospheric correction techniques, *Remote Sens. Environ.*, *170*, 40–47.

Bekaert, D., A. Hooper, and T. Wright (2015b), Reassessing the 2006 Guerrero slow-slip event, Mexico: Implications for large earthquakes in the Guerrero Gap, *J. Geophys. Res. Solid Earth*, *120*, 1357–1375, doi:10.1002/2014JB011557.

Caricchi, L., J. Biggs, C. Annen, and S. Ebmeier (2014), The influence of cooling, crystallisation and re-melting on the interpretation of geodetic signals in volcanic systems, *Earth Planet. Sci. Lett.*, *388*, 166–174.

Chi, S., and R. Reilinger (1984), Geodetic evidence for subsidence due to groundwater withdrawal in many parts of the United States of America, *J. Hydrol.*, *67*(1), 155–182.

Clifton, A., F. Sigmundsson, K. Feigl, G. Guðmundsson, and T. Árnadóttir (2002), Surface effects of faulting and deformation resulting from magma accumulation at the Hengill triple junction, SW Iceland, 1994–1998, *J. Volcanol. Geotherm. Res.*, *115*, 233–255.

Decriem, J., et al. (2010), The 2008 May 29 earthquake doublet in SW Iceland, *Geophys. J. Int.*, *181*, 1128–1146.

DeMets, C., R. G. Gordon, and D. F. Argus (2010), Geologically current plate motions, *Geophys. J. Int.*, *181*(1), 1–80.

Drouin, V. (2016), Constraints on deformation processes in Iceland from space geodesy: Seasonal load variations, plate spreading, volcanoes and geothermal fields, PhD thesis, Faculty of Earth Sci., Univ. of Iceland, Reykjavik, Iceland.

Dzurisin, D. (2007), *Volcano Deformation*, Springer, Berlin.

Efron, B., and R. Tibshirani (1986), Bootstrap methods for standard errors, confidence intervals, and other measures of statistical accuracy, *Stat. Sci.*, *1*(1), 54–75.

Einarsson, P. (1991), Earthquakes and present-day tectonism in Iceland, *Tectonophysics*, *189*(1), 261–279.

Einarsson, P. (2008), Plate boundaries, rifts and transforms in Iceland, *Jokull*, *58*(12), 35–58.

Eshelby, J. D. (1957), The determination of the elastic field of an ellipsoidal inclusion, and related problems, *Proc. R. Soc. A*, *241*, 376–396, The Royal Society.

Eysteinsson, H. (2000), Elevation and gravity changes at geothermal fields on the Reykjanes Peninsula, SW Iceland, paper presented at 2000 World Geothermal Congress, pp. 559–564, Kyushu-Tohoku, Japan, 28 May–10 Jun.

Feigl, K. L., J. Gasperi, F. Sigmundsson, and A. Rigo (2000), Crustal deformation near Hengill volcano, Iceland 1993–1998: Coupling between magmatic activity and faulting inferred from elastic modeling of satellite radar interferograms, *J. Geophys. Res.*, *105*(25), 655–25.

Fialko, Y., and M. Simons (2000), Deformation and seismicity in the Coso geothermal area, Inyo County, California: Observations and modeling using satellite radar interferometry, *J. Geophys. Res.*, *105*, 21,781–21,793.

Fielding, E., R. Blom, and R. Goldstein (1998), Rapid subsidence over oil fields measured by SAR interferometry, *Geophys. Res. Lett.*, *25*, 3215–3218.

Franzson, H., E. Gunnlaugsson, K. Árnason, K. Sæmundsson, B. Steingrímsson, and B. Harðarson (2010), The Hengill geothermal system, conceptual model and thermal evolution, paper presented at 2010 World Geothermal Congress, Bali, Indonesia, 25–29 Apr.

Geirsson, H., et al. (2010), Overview of results from continuous GPS observations in Iceland from 1995 to 2010, *Jokull*, *60*, 3–22.

Gunnarsson, G., A. Arnaldsson, and A. Oddsdóttir (2011), Model simulations of the Hengill Area, southwestern Iceland, *Transp. Porous Media*, *90*, 3–22.

Gunnlaugsson, E. (2016a), Nesjavellir–vinnsluskýrsla 2015, *Tech. Rep.*, Orkuveita Reykjavíkur (Reykjavik Energy), Reykjavik, Iceland.

Gunnlaugsson, E. (2016b), Hellisheiði–vinnsluskýrsla 2015, *Tech. Rep.*, Orkuveita Reykjavíkur (Reykjavik Energy), Reykjavik, Iceland.

Halldorsson, B., S. Olafsson, J. T. Snaebjörnsson, S. Sigurðsson, R. Rupakhety, and R. Sigbjörnsson (2012), On the effects of induced earthquakes due to fluid injection at Hellisheidi Geothermal Power Plant, Iceland, paper presented at 15th WCEE, Lissabon, Portugal.

Haraldsdóttir, S. H. (2014), Mælingareftirlit á vinnslusvæðum Hellisheiðarvirkjunar árið 2014, *Tech. Rep. 2014/052*, ÍSOR, Reykjavik, Iceland.

Hastings, W. K. (1970), Monte Carlo sampling methods using Markov chains and their applications, *Biometrika*, *57*(1), 97–109.

Herring, T., R. W. King, M. A. Floyd, and S. C. McClusky (2015), Introduction to GAMIT/GLOBK, release 10.6, Tech. Rep., Mass. Inst. Technol., Cambridge, Mass.

Hooper, A. (2008), A multi-temporal insar method incorporating both persistent scatterer and small baseline approaches, *Geophys. Res. Lett.*, *35*, L16302, doi:10.1029/2008GL034654.

Hooper, A., D. Bekaert, K. Spaans, and M. Arıkan (2012), Recent advances in SAR interferometry time series analysis for measuring crustal deformation, *Tectonophysics*, *514*, 1–13.

Hreinsdóttir, S., T. Árnadóttir, J. Decriem, H. Geirsson, A. Tryggvason, R. Bennett, and P. LaFemina (2009), A complex earthquake sequence captured by the continuous GPS network in SW Iceland, *Geophys. Res. Lett.*, *36*, L12309, doi:10.1029/2009GL038391.

Hurwitz, S., L. B. Christiansen, and P. A. Hsieh (2007), Hydrothermal fluid flow and deformation in large calderas: Inferences from numerical simulations, *J. Geophys. Res.*, *112*, B02206, doi:10.1029/2006JB004689.

Hutnak, M., S. Hurwitz, S. Ingebritsen, and P. Hsieh (2009), Numerical models of caldera deformation: Effects of multiphase and multicomponent hydrothermal fluid flow, *J. Geophys. Res.*, *114*, B04411, doi:10.1029/2008JB006151.

Jakobsdóttir, S. S. (2008), Seismicity in Iceland: 1994–2007, *Jokull*, *58*, 75–100.

Jeanne, P., J. Rutqvist, D. Vasco, J. Garcia, P. F. Dobson, M. Walters, C. Hartline, and A. Borgia (2014), A 3D hydrogeological and geomechanical model of an enhanced geothermal system at the Geysers, California, *Geothermics*, *51*, 240–252.

Jónsson, S., H. Zebker, P. Segall, and F. Amelung (2002), Fault slip distribution of the 1999 M_w 7.1 Hector Mine, California, earthquake, estimated from satellite radar and GPS measurements, *Bull. Seismol. Soc. Am.*, *92*(4), 1377–1389.

Kampes, B. M., R. F. Hanssen, and Z. Perski (2003), Radar interferometry with public domain tools, paper presented at 3rd International Workshop on ERS SAR Interferometry, 'FRINGE03', p. 6, Frascati, Italy.

Keiding, M., T. Árnadóttir, S. Jónsson, J. Decriem, and A. Hooper (2010), Plate boundary deformation and man-made subsidence around geothermal fields on the Reykjanes Peninsula, Iceland, *J. Volcanol. Geotherm. Res.*, *194*, 139–149.

Kirkpatrick, S., C. Gelatt, and M. P. Vecchi (1983), Optimization by simulated annealing, *Science*, *220*(4598), 671–680.

Metropolis, N., A. W. Rosenbluth, M. N. Rosenbluth, A. H. Teller, and E. Teller (1953), Equation of state calculations by fast computing machines, *J. Chem. Phys.*, *21*(6), 1087–1092.

Minson, S., M. Simons, and J. Beck (2013), Bayesian inversion for finite fault earthquake source models I—Theory and algorithm, *Geophys. J. Int.*, *194*, 1701–1726.

Mogi, K. (1958), Relations between the eruptions of various volcanoes and the deformations of the ground surfaces around them, *Bull. Earthquake Res. Inst. Univ. Tokyo*, *36*, 99–134.

Mossop, A., and P. Segall (1997), Subsidence at the Geysers geothermal field N. California from a comparison of GPS and leveling surveys, *Geophys. Res. Lett.*, *24*(14), 1839–1842.

Pedersen, R., S. Jónsson, T. Árnadóttir, F. Sigmundsson, and K. L. Feigl (2003), Fault slip distribution of two June 2000 M_w 6.5 earthquakes in South Iceland estimated from joint inversion of InSAR and GPS measurements, *Earth Planet. Sci. Lett.*, *213*(3), 487–502.

Robertson, E. C. (1988), Thermal properties of rocks, *88–441*, US Geol. Surv., Reston, Va.

Sæmundsson, K. (1967), Vulkanismus und Tektonik des Hengill-Gebietes in SW-Island, *Acta Nat. Isl.*, *2*, 105.

Segall, P. (1985), Stress and subsidence resulting from subsurface fluid withdrawal in the epicentral region of the 1983 Coalinga earthquake, *J. Geophys. Res.*, *90*(B8), 6801–6816.

Sigmundsson, F., P. Einarsson, S. Røgnvaldsson, G. Foulger, K. Hodgkinson, and G. Thorbergsson (1997), The 1994–1995 seismicity and deformation at the Hengill triple junction, Iceland: Triggering of earthquakes by minor magma injection in a zone of horizontal shear stress, *J. Geophys. Res.*, *102*, 15,151–15,161.

Tryggvason, A., S. T. Rögnvaldsson, and O. G. Flóvenz (2002), Three-dimensional imaging of the *P*-and *S*-wave velocity structure and earthquake locations beneath Southwest Iceland, *Geophys. J. Int.*, *151*(3), 848–866.

Tryggvason, H. (2014), Mælingareftirlit á Nesjavöllum árið 2014, *Tech. Rep. 2014/060*, ÍSOR, Reykjavik, Iceland.

Turcotte, D. L., and G. Schubert (2002), *Geodynamics*, 2nd ed., Cambridge Univ. Press, Cambridge, U. K.

Vasco, D. W., J. Rutqvist, A. Ferretti, A. Rucci, F. Bellotti, P. Dobson, C. Oldenburg, J. Garcia, M. Walters, and C. Hartline (2013), Monitoring deformation at the Geysers Geothermal Field, California using C-band and X-band interferometric synthetic aperture radar, *Geophys. Res. Lett.*, *40*, 2567–2572, doi:10.1002/grl.50314.

Vogfjörd, K., and R. Slunga (2003), Rupture in the South Iceland Seismic Zone forced by magmatic intrusion in the Hengill area, Abstract 9685 presented at 2003 EGS-AGU-EUG Joint Assembly, vol. 1, Nice, France, 6–11 Apr.

Wessel, P., and W. Smith (1991), Free software helps map and display data, *Eos Trans. AGU*, *72*(41), 445–446.

Wessel, P., W. Smith, R. Scharroo, J. Luis, and F. Wobbe (2013), Generic mapping tools: Improved version released, *Eos Trans. AGU*, *94*(45), 409–410.

Yang, X. M., P. M. Davis, and J. H. Dieterich (1988), Deformation from inflation of a dipping finite prolate spheroid in an elastic half-space as a model for volcanic stressing, *J. Geophys. Res.*, *93*(B5), 4249–4257.